

# Numerical Investigation of Flow-induced Noise Generation at the Nozzle End of Jet Engines

Andreas Babucke, Markus Kloker, and Ulrich Rist

Institut für Aerodynamik und Gasdynamik, Universität Stuttgart  
Pfaffenwaldring 21, D-70550 Stuttgart, Germany  
✉ babucke@iag.uni-stuttgart.de  
<http://www.iag.uni-stuttgart.de>

## Summary

Sound generation downstream the nozzle end of a subsonic laminar jet has been investigated using two-dimensional direct numerical simulations (DNS). The nozzle end is modeled by a finite flat plate with Mach numbers of  $Ma_I = 0.8$  above and  $Ma_{II} = 0.2$  below the splitter plate. Behind the nozzle end, a combination of a wake and mixing layer develops. Due to the high amplification rates, disturbances saturate before a pure mixing layer occurs. Non-linear generation mechanisms produce higher harmonic disturbances in the upper boundary layer, resulting in an only quasi periodic solution. The main acoustic sources correspond to the positions of vortex pairing. Broadband noise is emitted instead of tonal noise, known from the pure mixing layer without a splitter plate [4].

## 1 Introduction

Noise reduction is an important issue for a wide range of technical problems but the mechanisms of flow-induced sound are not yet understood properly. The current investigation focuses on jet noise as it is a major noise source of aircrafts. Aero-acoustic simulations are a relatively new field in computational fluid dynamics demanding high requirements in computational performance and the accuracy of the computational scheme itself. On the one hand, a high resolution is needed to compute the noise sources accurately, on the other hand, it demands a large computational domain to obtain the relevant portions of the acoustic far-field. As the acoustic amplitudes are small compared to the flow-field disturbances, boundary conditions have to be chosen carefully, in order not to spoil the acoustic field with reflections.

Previous investigations of jet noise have been focusing on either pure mixing layers [3, 4] or low Reynolds number jets [5], where a S-shaped velocity profile is used at the inflow. In this two-dimensional DNS, we include the nozzle end, modeled by a thin flat plate with two different free-stream velocities on top and below. This allows to investigate the influence of the wake formed by the two boundary layers. Additionally, the splitter plate gives the possibility to model real actuators for future noise reduction instead of unrealistic volume forcing.

## 2 Computational Configuration

### 2.1 Numerical Method

The two-dimensional simulation is a first step and has been performed using the NS3D code [2]. It solves the unsteady compressible Navier-Stokes equations. The code is written in conservative formulation, solving for density  $\rho$ , the momentum densities  $\rho u$ ,  $\rho v$  and the total energy per volume  $E$ . The velocity components are normalized by the inflow velocity  $\bar{U}_\infty$ , the pressure with  $\bar{p} \cdot \bar{U}_\infty^2$  and all other quantities by their inflow values of the upper boundary layer (see figure 1), marked with the subscript  $\infty$ . Length scales are made dimensionless with a reference length  $\bar{L}$  and the time with  $\bar{L}/\bar{U}_\infty$ , where the overbar denotes dimensional quantities. The viscosity is modeled using the Sutherland law with a reference viscosity  $\bar{\mu}(\bar{T}_\infty = 280K) = 1.735 \cdot 10^{-5} kg/(ms)$ . Since we can assume a weak temperature dependence, the Prandtl number  $Pr = 0.71$  and the ratio of specific heats  $\kappa = 1.4$  are taken constant.

In streamwise ( $x$ ) and normal ( $y$ ) direction, the flow-field is discretized by 6<sup>th</sup>-order compact finite differences. Alternating up- and downwind-biased differences [7] are applied to convective terms for de-aliasing. Second derivatives are computed directly instead of applying the first derivative twice. This leads to better resolved viscous terms and improves the stability of the code [1]. Grid transformation in the  $x$ - $y$  plane is implemented by mapping the physical grid on an equidistant computational  $\xi$ - $\eta$  grid. The equations are integrated in time using the standard 4<sup>th</sup>-order Runge-Kutta scheme. The domain decomposition in the  $x$ - $y$  plane is not only used for parallelization, it also allows to define neighbours or specific boundary conditions for each domain. Therefore, the nozzle end can be included easily without any special treatment of corner points.

At the free stream boundaries, a one-dimensional characteristic boundary condition [6] is used. An additional damping zone forces the flow variables smoothly to a steady state solution. Prescribing amplitude and phase distributions from linear stability theory allows to introduce defined disturbances at the subsonic inflow with characteristic boundary conditions [6]. The outflow is the most crucial part as one has to avoid large structures passing the boundary and contaminating the acoustic field. Therefore, a combination of grid stretching and spatial low-pass filtering is applied in the sponge region. Disturbances become increasingly badly resolved as they propagate through the sponge region. As the spatial filter depends on the step size in  $x$ -direction, perturbations are smoothly dissipated before they reach the outflow boundary. This procedure shows very low reflections and has been already applied by Colonius et al. [4].

### 2.2 Flow parameters

For the current investigation, an isothermal subsonic jet with the Mach numbers  $Ma_I = 0.8$  for the upper and  $Ma_{II} = 0.2$  for the lower stream has been selected. As both temperatures are equal ( $T_1 = T_2 = 280K$ ), the ratio of the streamwise

velocities is  $U_I/U_{II} = 4$ . This large factor leads to strong instabilities behind the nozzle end, so a moderate number of grid points in x-direction is sufficient to simulate the aeroacoustic source. The Reynolds number  $Re = \rho_\infty U_1 \delta_{1,I} / \mu_\infty = 1000$  is based on the displacement thickness  $\delta_{1,I}$  of the upper stream at the inflow. With  $\delta_{1,I}(x_0) = 1$ , length scales are normalized with the displacement thickness of the fast stream at the inflow. The boundary layer of the lower stream corresponds to the same origin of the flat plate.

The cartesian grid is decomposed into eight subdomains, four in streamwise and two in normal direction. Each subdomain contains  $650 \times 425$  points in  $x$ - and  $y$ -direction. The mesh is uniform in streamwise direction with a step size of  $\Delta x = 0.15$  up to the sponge region, where the grid is highly stretched. In normal direction, the finest step size is  $\Delta y = 0.15$  in the middle of the domain with a continuous stretching up to a spacing of  $\Delta y = 1.06$ . The origin of the coordinate system ( $x = 0$ ,  $y = 0$ ) is located at the end of the nozzle. The nozzle end is modeled by a finite thin flat plate with a thickness of one  $\Delta y$ . Due to the vanishing thickness of the nozzle end, an isothermal boundary condition at the wall has been chosen. The temperature of the plate is  $\bar{T}_{wall} = 296K$ , being the mean value of the adiabatic wall temperatures of the two streams.

The initial condition along the flat plate is obtained from similarity solutions of the boundary-layer equations. Further downstream, the full boundary-layer equations are integrated downstream, providing a flow-field sufficient for an initial condition and linear stability theory. The resulting streamwise velocity profiles of the initial condition are shown in figures 1 and 2. Behind the nozzle end, the flow field keeps its wake-like shape for a long range. As high amplification rates occur here, the flow is already unsteady before a pure mixing layer has developed. This means that the pure mixing layer investigated earlier [1, 3, 4] has to be considered as a rather theoretical approach.

### 3 Linear Stability Theory

Spatial linear stability theory (LST) is used both to introduce disturbances at the inflow, as well as for further analysis of the flow-field. As the flow is highly unsteady behind the nozzle end and enforcing an artificial steady state does not work properly, we use the initial condition derived from the boundary-layer equations to compute eigenvalues and eigenfunctions. The computation is based on a 4<sup>th</sup>-order matrix solver combined with Wielandt iteration. According to figure 3, a fundamental angular frequency of  $\omega = 0.0688$  was chosen for the upper boundary layer. The amplification keeps almost constant in downstream direction. As the two boundary layers emerge from the same position, the lower boundary layer is stable up to the nozzle end. Behind the edge of the splitter plate, amplification rates 50 times higher than in the upper boundary layer occur due to the inflection points of the streamwise-velocity profile. Maximum amplification in the mixing layer takes place for a frequency of roughly three to four times of the fundamental frequency of the boundary layer as illustrated in figure 4.

## 4 Numerical Results

The flow is forced at the inflow of the upper boundary layer with a single disturbance of the fundamental frequency  $\omega_0$  and an amplitude of  $u'_{max} = 5 \cdot 10^{-3}$ , using the corresponding eigenfunction from linear stability theory. As the flow field is only quasi periodic in time, a time interval of 64 fundamental periods with a sampling rate of 4000 timesteps is used for analysis. To ensure that no initial disturbances falsify the results, a total number of 556000 timesteps, corresponding to 139 periods of the fundamental frequency, has been computed. As the maxima of  $u$ -disturbances in the boundary layer are located near the wall, analysis of amplitudes is mainly based on the maximum of the streamwise velocity along  $y$ . Thus only a small data strip in  $y$ -direction with high temporal resolution is required for postprocessing. The spatial growth rates  $\alpha_i$  are compared with linear stability theory in figures 5 and 6 for the upper boundary layer and the following mixing layer, respectively. For the latter, the normal velocity  $v$  is chosen as it is mainly associated with vorticity and does not contain upstream propagating sound. The maximum amplitudes of the streamwise velocity  $u$  are shown in figure 7 where the fundamental frequency and its first five higher harmonics are highlighted. Note that along the splitter plate ( $x \leq 0$ ), the values of the upper boundary layer are used.

In the upper boundary layer, the fundamental disturbance  $(1, 0)$  behaves according to linear stability theory. The amplification rates of the first two higher harmonics  $(2, 0)$  and  $(3, 0)$  approach the one of the fundamental frequency, indicating that they are generated by the fundamental disturbance. Near the end of the splitter plate ( $-20 < x < 10$ ), the growth rates differ from linear stability results due to the discontinuity in geometry at  $x = 0$ . The amplitudes of the streamwise velocity  $u$  shown in figure 7 reveal the generation of higher harmonics in the upper boundary layer, leading to a wider disturbance spectrum for the subsequent mixing layer.

Behind the splitter plate, the first three higher harmonics are now strongly amplified and grow according to linear stability theory (figure 6). Due to increased amplitudes of several frequencies, also originally stable modes grow now caused by non-linear interaction of the amplified disturbances. With many disturbances having large amplitudes, only a quasi periodic solution can be reached. Saturation of the second higher harmonic  $(3, 0)$  takes place at  $x \approx 60$ . In figure 8, we can see that this is the position where the mixing layer rolls up and the first vortex is generated. Further downstream, the lower frequencies  $(1, 0)$  and  $(2, 0)$  dominate the flow field, corresponding to subsequent vortex pairing. At  $x = 150$ , two out of three eddies pair and the resulting vortex merges with the remaining eddy at  $x = 220$ . Thereby, it is only quasi-deterministic whether the single eddy pairs with the precedent or subsequent bigger vortex.

The resulting emitted sound is visualized by the dilatation field  $\nabla \vec{u}$  together with the spanwise vorticity in figure 9. Although the sound generation is less clear than for a pure mixing layer [4], the dilatation field allows to determine roughly two acoustic sources. Their positions correspond to the locations of vortex pairing mentioned above. By placing an observer in the acoustic field ( $x = 195, y = -121.8$ ), the emitted sound can be evaluated more precisely. Looking at the time dependent

pressure signal in figure 10, almost random fluctuations can be observed. The spectrum of the acoustic pressure in figure 11 shows a broadband noise with decaying amplitudes for higher frequencies. Despite the full spectrum, peaks at higher harmonics of the fundamental frequency ( $\omega/\omega_0 = 2, 3, 4, 6$ ) can be observed.

## 5 Conclusion

The nozzle end of an isothermal jet with Mach numbers  $Ma_I = 0.8$  and  $Ma_{II} = 0.2$  has been simulated using two-dimensional DNS. As a model for the nozzle end of a jet, the mixing of two co-floating streams downstream of a splitter plate is used. The baseflow obtained from the boundary-layer equations shows a combination of wake and mixing layer behind the nozzle end. The flow becomes highly unsteady already before a pure mixing layer develops. As the disturbances saturate, roll up of the mixing layer and, further downstream, vortex pairing occurs. Due to large amplitudes, non-linear mechanisms produce a wide spectrum of disturbances, leading to a less deterministic flow-field as it is the case for the pure mixing layer. This results in a broadband noise emission, still showing peaks at the higher harmonics in the pressure spectrum. Further investigations will include three-dimensional simulations and the development of actuators for noise reduction.

## Acknowledgements

The authors would like to thank the Deutsche Forschungsgemeinschaft (DFG) for its financial support within the subproject SP5 in the research group FOR-508 "Noise Generation in Turbulent Flows". Supercomputing time was provided by the Höchstleistungsrechenzentrum Stuttgart (HLRS) within the projects "Lamtur" and "Teraflop Workbench".

## References

- [1] A. Babucke, M. J. Kloker, and U. Rist. DNS of a plane mixing layer for the investigation of sound generation mechanisms. *to appear in Computers and Fluids*, 2006.
- [2] A. Babucke, J. Linn, M. J. Kloker, and U. Rist. Direct numerical simulation of shear flow phenomena on parallel vector computers. In *High performance computing on vector systems: Proceedings of the High Performance Computing Center Stuttgart 2005*. Springer Verlag Berlin, 2006.
- [3] C. Bogey, C. Bailly, and D. Juve. Numerical simulation of sound generated by vortex pairing in a mixing layer. *AIAA J.*, 38(12):2210–2218, 2000.
- [4] T. Colonius, S. K. Lele, and P. Moin. Sound generation in a mixing layer. *J. Fluid Mech.*, 330:375–409, 1997.
- [5] J. B. Freund. Noise sources in a low-Reynolds-number turbulent jet at Mach 0.9. *J. Fluid Mech.*, 438:277–305, 2001.
- [6] M. B. Giles. Nonreflecting boundary conditions for Euler equation calculations. *AIAA J.*, 28(12):2050–2058, 1990.
- [7] M. J. Kloker. A robust high-resolution split-type compact FD scheme for spatial DNS of boundary-layer transition. *Appl. Sci. Res.*, 59:353–377, 1998.

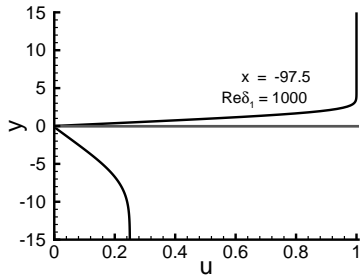


**Figure 1** Profile of the streamwise velocity  $u$  for the upper and lower boundary layer at the inflow.

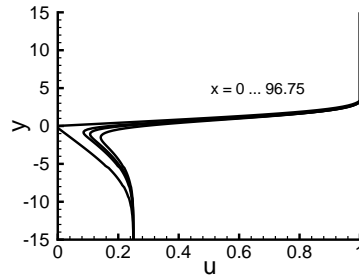


**Figure 2** Downstream evolution of the streamwise velocity profile behind the nozzle end.

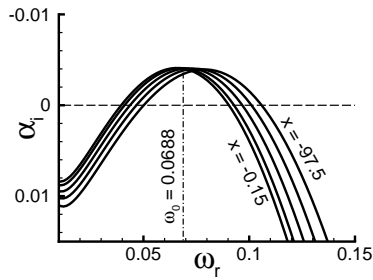


**Figure 3** Amplification rates of the upper (fast) boundary layer given by linear stability theory for various  $x$ -positions.

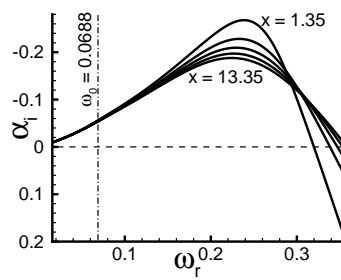


**Figure 4** Amplification rates for various  $x$ -positions behind the splitter plate predicted by linear stability theory.

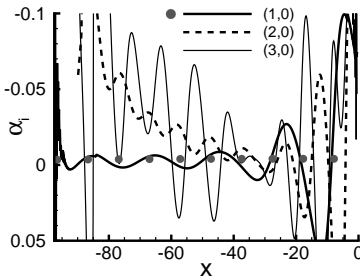


**Figure 5** Amplification rates of streamwise velocity  $u$  in the upper boundary layer, based on maximum amplitudes along  $y$ . Symbols denote results from linear stability theory.

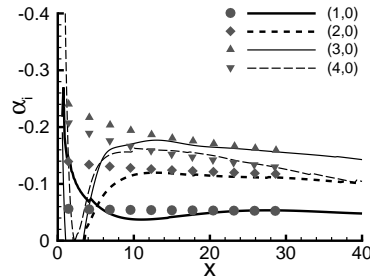


**Figure 6** Amplification rates of normal velocity  $v$  behind the nozzle end, based on maximum amplitudes along  $y$ . Symbols denote results from linear stability theory.

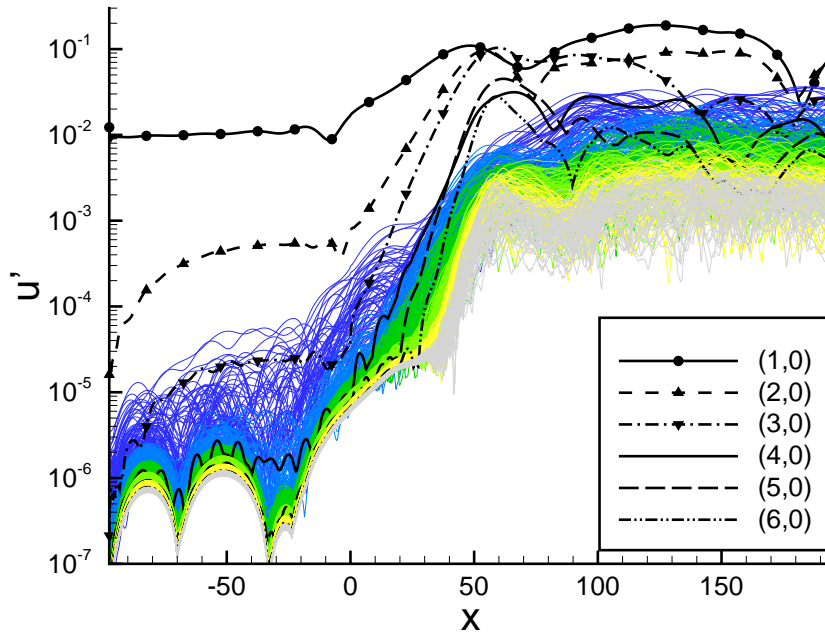


**Figure 7** Maximum amplitude of the streamwise velocity fluctuation  $u'$  in the upper boundary layer ( $x < 0$ ) and behind the splitter plate ( $x \geq 0$ ). The fundamental frequency and its five higher harmonics are plotted in bold and labeled separately. The non-integer higher harmonics are colored in dark and bright blue, dark and bright green, yellow and grey, respectively. Each color corresponds to a frequency range of  $1 \cdot \omega_0$ .  $(h, 0)$  means frequency  $h \cdot \omega_0$  with zero spanwise wavenumber.

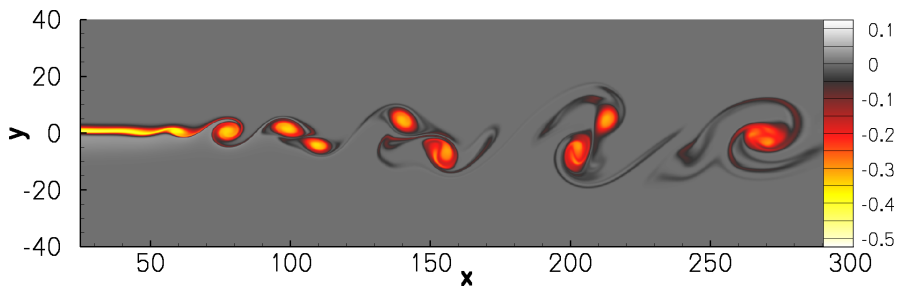


**Figure 8** Snapshot of the spanwise vorticity behind the nozzle end (located at  $x = 0$ ). Contour levels range from  $-0.53$  to  $0.12$ .

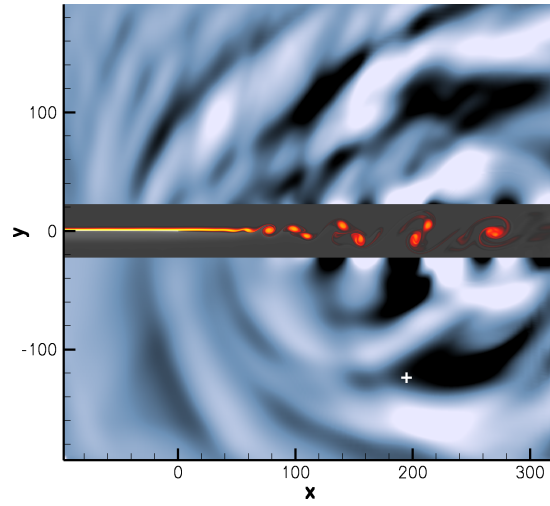


**Figure 9** Snapshot of the far-field sound showing the dilatation  $\nabla u$  in a range of  $\pm 3 \cdot 10^{-4}$ . The two boundary layers and the evolving mixing layer are illustrated by spanwise vorticity with the same contour levels as in figure 8. The position of the observer is marked by a white cross.

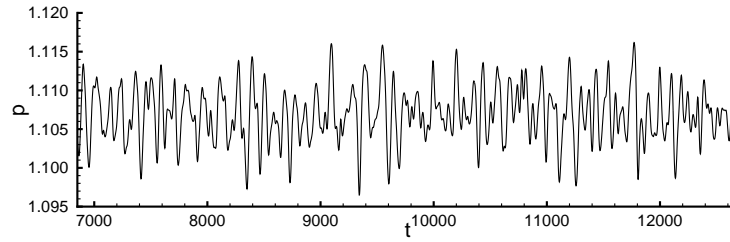


**Figure 10** Time-dependent signal of the acoustic pressure fluctuations in the far-field at the observer's position ( $x = 195, y = -121.8$ ).

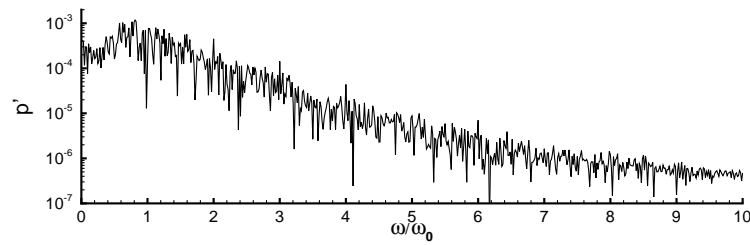


**Figure 11** Amplitude spectrum of the acoustic pressure relative to the fundamental frequency at the observer's position ( $x = 195, y = -121.8$ ). Analysis is based on the time frame shown in figure 10.